Green Chemistry

PAPER

Check for updates

Cite this: *Green Chem.*, 2023, **25**, 10485

Avoiding solid carbon deposition in plasma-based dry reforming of methane†

Omar Biondo, *[a,b] Cas F. A. M. van Deursen,[b] Ashley Hughes,[b,c] Alex van de Steeg,[b] Waldo Bongers,[b] M. C. M. van de Sanden,[b,d] Gerard van Rooij[b,e] and Annemie Bogaerts [a]

Received 23rd September 2023,
Accepted 23rd November 2023

DOI: 10.1039/d3gc03595f

rsc.li/greenchem

Solid carbon deposition is a persistent challenge in dry reforming of methane (DRM), affecting both classical and plasma-based processes. In this work, we use a microwave plasma in reverse vortex flow configuration to overcome this issue in CO_2/CH_4 plasmas. Indeed, this configuration efficiently mitigates carbon deposition, enabling operation even with pure CH_4 feed gas, in contrast to other configurations. At the same time, high reactor performance is achieved, with CO_2 and CH_4 conversions reaching 33% and 44% respectively, at an energy cost of 14 kJ L^{-1} for a $CO_2:CH_4$ ratio of 1 : 1. Laser scattering and optical emission imaging demonstrate that the shorter residence time in reverse vortex flow lowers the gas temperature in the discharge, facilitating a shift from full to partial CH_4 pyrolysis. This underscores the pivotal role of flow configuration in directing process selectivity, a crucial factor in complex chemistries like CO_2/CH_4 mixtures and very important for industrial applications.

Introduction

Plasma-based dry reforming of methane (DRM),[1,2] *i.e.*, the combined conversion of CO_2 and CH_4, is an attractive solution to electrify the energy-intensive production of syngas (H_2 + CO), as essential building block for the synthesis of hydrocarbons through Fischer–Tropsch[3] or oxygenates (*e.g.* methanol[4]). Its full exploitation is hampered by solid carbon deposition inside the reactor, leading to unstable operations (*e.g.*, due to microwave absorption in microwave discharges[5,6] or by creating conductive layers inside the reactor body[7]) and limiting the CH_4/CO_2 ratio to ≤ 1 under most experimental conditions.[1,2] In effect, solid carbon formation plays a central role in industrial-scale plasma arc technologies, such as the "Hüls process" to convert CH_4 into C_2H_2 and H_2, and the "Kværner process" for CH_4 pyrolysis into carbon black and H_2.[8] In addition, solid carbon formation limits the possibility of coupling the plasma exhaust with a catalytic bed (*e.g.*, to exploit the heat losses from the plasma zone), leading to "coking" deactivation of the catalyst.[9,10] However, Lašič Jurković *et al.*[11] demonstrated that a Ni/Al_2O_3 catalyst could be coupled with a spark discharge without incurring catalyst coking when the CH_4 fraction in the feed gas is well below 50% (*i.e.* approx. 33%). The authors suggested that stable operations could be expanded towards more CH_4-rich mixtures through reactor geometry optimization and by adding regeneration cycles with pure CO_2 feed gas. In another work, Lašič Jurković *et al.*[12] observed a drastic reduction in the production of oxygenates during the partial oxidation of methane in a dielectric barrier discharge coupled with zeolites. The formation of carbon in these materials was attributed to pronounced degradation of products due to long residence times in the zeolite pores and local electric field enhancement. Using metals that inhibit the formation of metal-carbide bonds can avoid coking deactivation and prolong the stability of plasma-catalytic operations.[10] However, these measures to reduce coking at the catalyst bed cannot mitigate the effect of gas-phase reactions contributing to solid carbon deposition.

Indeed, in DRM, solid carbon is primarily formed as a consequence of gas-phase, homogeneous pyrolytic reactions, especially C_2 hydrocarbon pyrolysis,[13] enhanced by O and OH radicals.[14] Hydrocarbon pyrolysis is endothermic and, therefore, promoted by the gas temperature (T_g) and gas residence time in the reaction zone.[13] Notably, previous research on plasma-based DRM suggested a correlation between the emergence of solid carbon and the specific energy input (SEI),

[a]*Research Group PLASMANT, Department of Chemistry, University of Antwerp, Universiteitsplein 1, Wilrijk B-2610, Belgium. E-mail: Omar.Biondo@uantwerpen.be*
[b]*DIFFER, 5612AJ Eindhoven, The Netherlands*
[c]*Department of Electrical Engineering and Electronics, University of Liverpool, Liverpool L69 3GJ, UK*
[d]*Department of Applied Physics, Eindhoven Institute for Renewable Energy Systems, P.O. Box 513, 5600 MB Eindhoven, The Netherlands*
[e]*Faculty of Science and Engineering, Maastricht University, 6229 GS Maastricht, The Netherlands*

†Electronic supplementary information (ESI) available: Details on the gas analysis, the volumetric production rates and the estimation of the plasma dimensions. See DOI: https://doi.org/10.1039/d3gc03595f

defined as the ratio of input power to feed flow rate, in various plasma sources.[7,15] This correlation suggests that solid carbon formation rises with SEI, attributed to a longer residence time and/or higher power, which directly influence T_g.

Microwave plasmas are expected to provide very good performance for DRM, with high selectivity towards syngas and high treatment capacity compared to other plasma sources, without compromising on energy efficiency.[1] Indeed, Chun *et al.*[16] achieved high conversion (68% and 97% for CO_2 and CH_4, respectively) and syngas concentration in the output of a $CO_2:CH_4$ 1 : 1 atmospheric microwave plasma torch, with a power input of 6 kW and a gas flow rate of 30 standard liters per minute (slm), corresponding to an SEI of 12 kJ L^{-1}. Nevertheless, the authors observed the release of solid carbon from the reactor body and did not report the carbon balance for their measurements. Subsequently, Sun *et al.*[17] tested a microwave reactor at lower power (2 kW) and flow rate (10 slm), but the same SEI (12 kJ L^{-1}), achieving very high conversion (91% and 96% for CO_2 and CH_4, respectively). In this case, the authors reported the presence of solid carbon on the inner wall of the reactor tube,[17] suggesting that the flow rate magnitude determines where solid carbon can be found (*i.e.* outside[16] or inside[17] the reactor). However, the flow rate does not determine whether solid carbon is found or not. Therefore, it is clear that the mechanism underlying solid carbon deposition is not yet understood, and the literature on CH_4/CO_2 microwave discharges is extremely limited.

Compared to microwave plasmas, arc discharges have been more often investigated for DRM.[1] In this class of plasma sources, the performance depends strongly on the reactor geometry. For instance, Dinh *et al.*[18] compared the performance of a conventional rotating arc reactor with a nozzle-type rotating arc reactor for N_2-assisted DRM ($CO_2:CH_4:N_2$ 2 : 6 : 8), reporting that the latter enhances both conversion and energy efficiency, thanks to improved heat transfer from the arc into gas activation and reduced heat losses to the walls. In the context of gliding arc discharges, optimization of the gas flow dynamics may enable improved performance, along with reduced carbon losses to solid products.[19] Liu *et al.*[20] could operate their forward vortex, gliding arc reactor at a CH_4/CO_2 = 0.67 ratio for nearly 2 h, with an SEI of 1.38 kJ L^{-1} and without severe carbon deposition. More recently, Van Alphen *et al.*[21] were able to increase the CH_4/CO_2 ratio to 1 in a reverse vortex, gliding arc reactor, while operating at a SEI of 3 kJ L^{-1}, with no operational issues reported. The ability of increasing the SEI while increasing the CH_4/CO_2 ratio suggests that the type of vortex stabilization affects carbon deposition at the reactor walls.

Up to now, the effect of the gas flow dynamics has never been studied in CH_4/CO_2 microwave discharges. In vortex-stabilized microwave plasmas, the cold outer vortex surrounding the hot plasma core facilitates rapid quenching of products, increasing the energy efficiency of the process.[22] In the commonly studied forward vortex flow configuration, quenching of products from the hot core is mainly provided by radial transport, as a result of temperature gradients as large as 5000 K cm^{-1}.[22] Nevertheless, the performance of a microwave plasma in forward vortex configuration suffers from weak control of the plasma core characteristics, due to suppression of convective core-periphery transport.[23]

In contrast, the reverse vortex flow configuration introduces a second inner vortex into the plasma zone, establishing convective core-periphery transport, a concept widely described in.[24] In this configuration, the tangential gas inlets and outlet are located on the same side of the plasma (Fig. 1). This results in an outer vortex flow along the reactor walls, and an inner vortex aimed at the opposite direction, as demonstrated for gliding arc plasmas.[25] The plasma is confined in the inner vortex, while the outer vortex provides near perfect heat insulation, as indeed shown for gliding arc plasmas.[24,25] Bongers *et al.*[26] were pioneers in investigating both forward and reverse vortex configurations in a sub-atmospheric pressure pure CO_2 microwave plasma. They reported a slightly higher energy efficiency in the reverse vortex at increasing pressure, peaking at around 500 mbar. Importantly, they observed that the energy efficiency reduction with increasing pressure is less pronounced compared to the forward vortex configuration. This observation hints at the potential for the reverse vortex configuration to offer enhanced energy-efficient CO_2 conversion even at atmospheric pressure. Nevertheless, this promising hypothesis remains untested thus far. In a notable step forward, van de Steeg[23] provided the first *in situ* characterization of a reverse vortex CO_2 microwave plasma. Their study highlighted how convective core-periphery transport enables control over residence time and T_g by adjusting the inlet gas flow rate. However, this approach has yet to be explored in complex chemistries, such as in DRM, where product selectivity is crucial. Therefore, we extrapolate from the above approach and apply it to the more complex chemistry of DRM, where product selectivity is generally assumed to be governed by gas residence time,[18] as also observed by Fincke *et al.*[27] for non-oxidative coupling of CH_4 to C_2H_2.

In this study, we demonstrate effective suppression of solid carbon deposition within a DRM microwave plasma operating in a reverse vortex flow configuration, even when utilizing pure CH_4 feed gas. While the commonly employed forward vortex configuration faces challenges of severe carbon deposition and discharge shutdown at CH_4 fractions >75%, the reverse vortex flow configuration emerges as a robust alternative. These observations, underpinned by *in situ* characterization of the discharge parameters through combined Raman-Thomson scattering, unveil the crucial role of the gas flow configuration in the solid carbon deposition process. In effect, this work overcomes the persistent challenge of carbon deposition and provides the insight in the underlying mechanism of flow dynamics as a means to control selectivity, which are both crucial for scaling up plasma-driven chemical processes.

Experimental

Plasma-laser scattering setup

The reactor configuration used in this work has been previously applied to pure CO_2 conversion in earlier studies and thoroughly described elsewhere.[23,28] In this study, we conduct

 This journal is © The Royal Society of Chemistry 2023

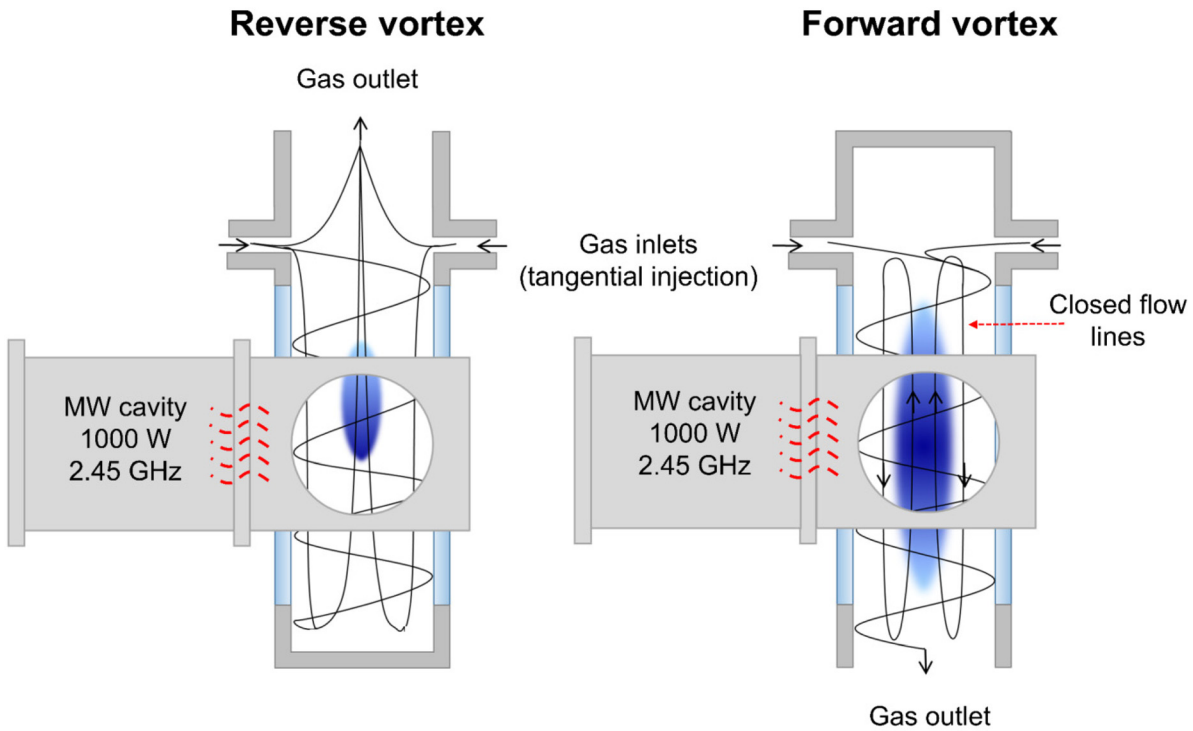

Fig. 1 Schematics of the reverse vortex and forward vortex flow configurations, with illustrations of flow lines based on Gutsol and Bakken.[24]

in situ characterization of both the reverse and forward vortex microwave plasma in a wide range of CO_2/CH_4 mixtures using a combination of rotational Raman and Thomson scattering. This approach provides quantitative measurements of the rotational (gas) temperature (assumed in equilibrium with T_g), as well as electron density and temperature, respectively.[29] We couple this laser scattering to a microwave plasma setup as schematically illustrated in Fig. 2.

A 2.45 GHz magnetron of 1 kW input power provides microwaves to the plasma, ignited in a quartz tube of 27 mm inner diameter. The quartz tube is positioned at a 90° angle from the long side of a WR340 waveguide. Optimal power transfer to the plasma is achieved by the combination of an adjustable short and EH tuner. CO_2 (99.995% purity) and CH_4 (4.5 grade) are premixed and tangentially injected into the reactor by two nozzles, located 100 mm upstream of the waveguide center. The tangential injection is used to create a swirl flow in the tube, protecting the walls from overheating and eventually melting, and the volumetric flow rate is fixed at 10 or 17 slm.

A frequency-doubled Nd:YAG laser (SpectraPhysics GCR-230, 30 Hz, 400 mJ per 10 ns pulse, 532 nm) is focused into the reactor along the axial direction and the scattered light is collimated and focused into a Littrow spectrometer. Attenuation of the intense Rayleigh scattered light and stray light is necessary to resolve Thomson and Raman signals. Therefore, a volume Bragg grating filter is placed before the entrance of the fiber array. The resulting spectrally resolved image is captured by an intensified camera (Princeton Instruments PI-MAX, 40 ns gate-width) after *ca.* 5 minutes from the ignition of the plasma. All measured images are corrected for the sensitivity of most optical components (camera, fibers, spectrometer), as calibrated with an integrating sphere. More details regarding the laser scattering setup, along with a discussion of the improvements introduced to the diagnostics, are available elsewhere.[23,29]

Optical emission imaging

Optical plasma emission is very suitable to reconstruct the plasma shape and estimate the discharge volume.[30,31] In this work, the plasma emission images are obtained using a CCD camera, as depicted in Fig. 3. The images are taken when the plasma has reached a steady state, *ca.* 5 minutes after ignition. The plasma light emission is filtered with a bandpass filter with a central wavelength of *ca.* 780 nm, aiming to simultaneously isolate the 777 nm $O(3s^5S^0 \leftarrow 3p^5P)$ spectral line emission and to capture the onset of the broadband emission (*ca.* 500–1100 nm, with a maximum at 800–900 nm) from hot carbon particles.[32–34] In this manner, optical emission imaging becomes a useful tool to trace the formation of carbon particles as precursors for carbon deposition in DRM, while keeping track of the change in emission distribution.

Gas chromatography

The exhaust composition is measured with a gas chromatograph (GC) (CompactGC 4.0 model – Interscience), positioned about 2 m downstream from the microwave cavity. The measurements were taken after *ca.* 5 minutes from plasma ignition, allowing for attainment of a steady-state output. N_2 is

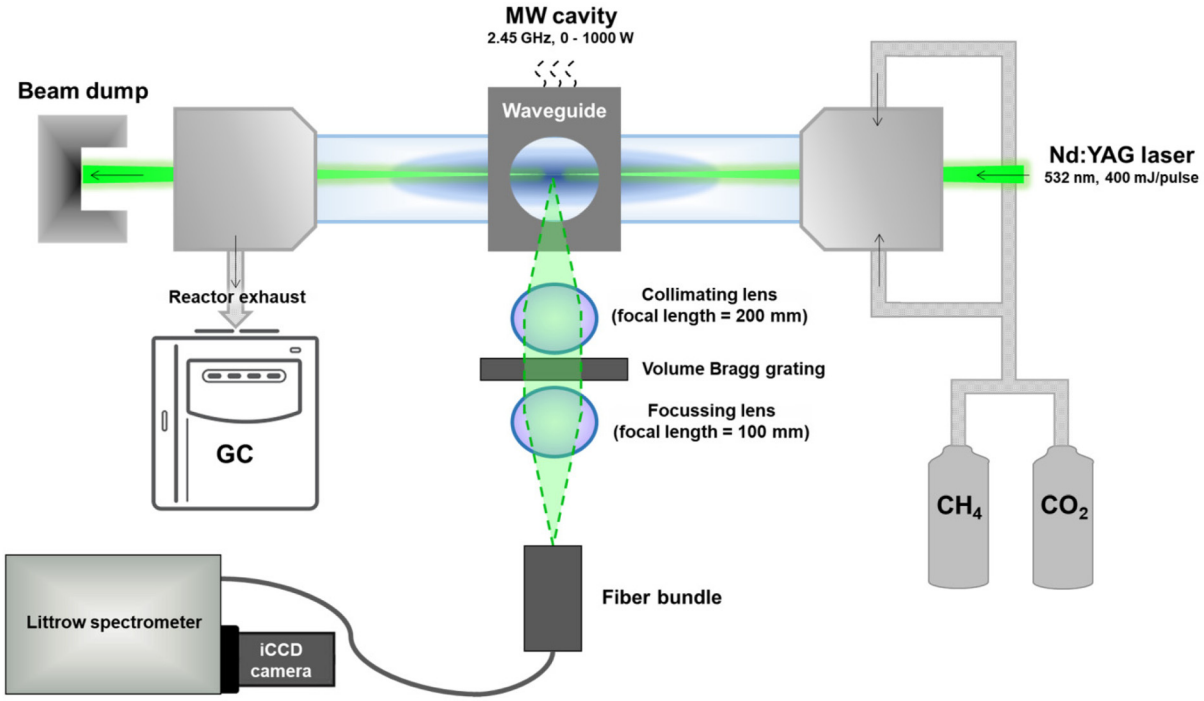

Fig. 2 Schematic of the combined plasma-laser scattering setup, with the microwave reactor in forward vortex flow configuration (see Fig. 1).

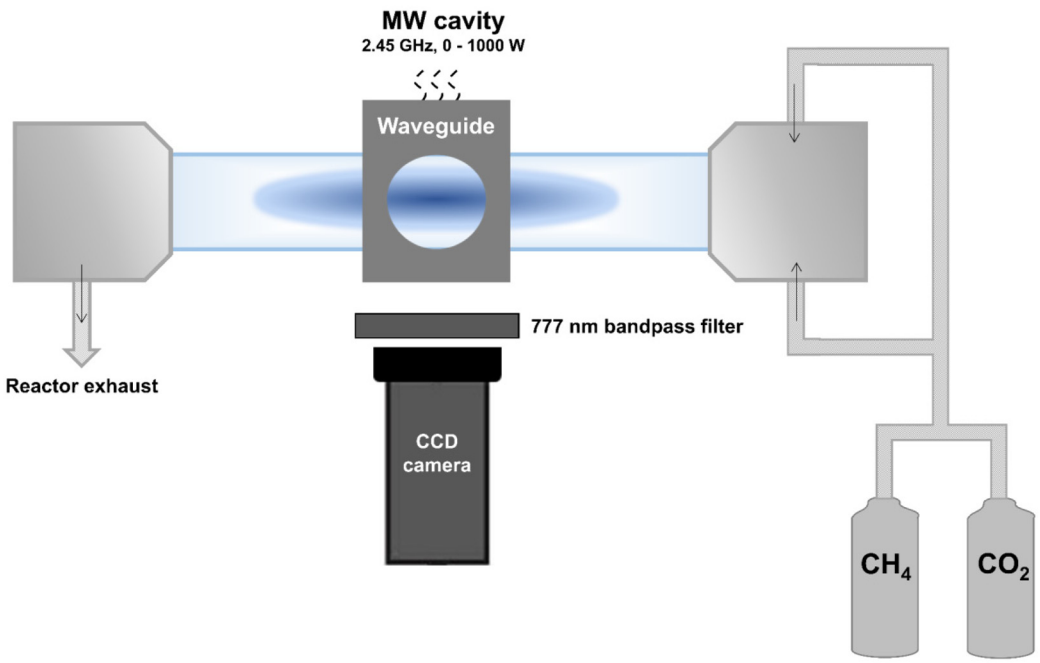

Fig. 3 Schematic of the combined plasma-optical emission setup, with the microwave reactor in forward vortex flow configuration (see Fig. 1).

added after the reactor outlet as internal standard to account for the flow rate changes between the reactor in- and outlet arising from *e.g.*, formation of dissociation products and removal of liquids, as detailed by Wanten *et al.*[2] and described in the ESI.† The gas flow going into the GC is dried using a MD-70-24 Nafion filter to prevent overflow of the liner and ensure peak separation, which could be compromised due to poor stationary phase wetting. Three injection loops are used for the detection of all components in the gas mixture. The first loop consists of an Rt-Q-Bond pre-column (4 m length,

 This journal is © The Royal Society of Chemistry 2023

0.32 mm ID) followed by a TC-Molsieve 5A (10 m length, 0.53 mm ID) column and a TCD detector for the detection of CO, N_2 and O_2. The second loop consists of an Rt-Q-Bond pre-column (2 m length, 0.32 mm ID) followed by a CP-PoraBOND Q column (20 m length, 0.32 mm ID) and a TCD detector for the detection of CO_2 and C_2H_2. The third loop consists of an Rt-Q-Bond column (3 m length, 0.32 mm ID) followed by a Molsieve 5A (10 m length, 0.53 mm ID) column and a TCD for detection of H_2. The molar composition of the gas is then obtained from the chromatograms using linear regression after calibrating the system. The procedure to correct the exhaust composition for the change in molar flow rate upon dissociation, N_2 addition and H_2O removal, and calculate the performance parameters presented and discussed in this study is detailed in the ESI.†

Results and discussion

Gas temperature and electron temperature and density

We characterize the CH_4/CO_2 20/80 microwave plasma using laser scattering to elucidate the transport phenomena, lying at the basis of solid carbon inhibition. The *in situ* characterization of the plasma for CH_4 fractions >20% in CO_2 is not yet possible due to the complexity of the chemical environment and the increase in C_2-Swan laser induced fluorescence,[35] which blends the Raman spectra. The results for the reverse and forward vortex configuration are compared in Fig. 4.

Fig. 4 shows that T_g is *ca.* 1500 K lower in reverse than in forward vortex configuration, leading to a larger difference between T_e and T_g, and thus a more pronounced non-equilibrium plasma in the reverse vortex configuration. On the other hand, the electron number density (n_e) and temperature (T_e) are in the same order of magnitude for both forward and reverse vortex configurations. The large error bars are ascribed to the overlap with the Rayleigh peak and the stray light that are cut from the spectra with a notch filter.[36,37]

The lower T_g of the reverse vortex flow configuration indicates that it enhances the heat removal from the core of the discharge, compared to the forward vortex configuration. This cooling effect is provided by a prominent convective flow established in the reverse vortex configuration, being absent in forward vortex configuration.[22,24] Therefore, the enhanced heat transport could lie at the basis of avoiding solid carbon deposition, but more experiments are needed to understand the mechanisms.

The effect of flow topology

Experiments in reverse vortex flow configuration feature solid carbon-free operations, even in pure CH_4. Our laser scattering results presented in the previous section suggest that there may be a link between a lower T_g in the core of the plasma and the inhibition of solid carbon deposition. Additional support to this hypothesis is provided by optical emission imaging, presented in Fig. 5.

Focusing first on the forward vortex configuration, Fig. 5 shows a sudden change in emission shape from 5% to 10% CH_4 in the feed gas, which reflects a transition from O 777 nm to carbon-dominated emission. Particularly, from 10% CH_4 onwards, the emission zone exhibits a cylindrical, hollow shape, as a result of the particle formation at the interface between the hot core and the cold outer vortex, as also reported in literature, albeit for completely different conditions.[33]

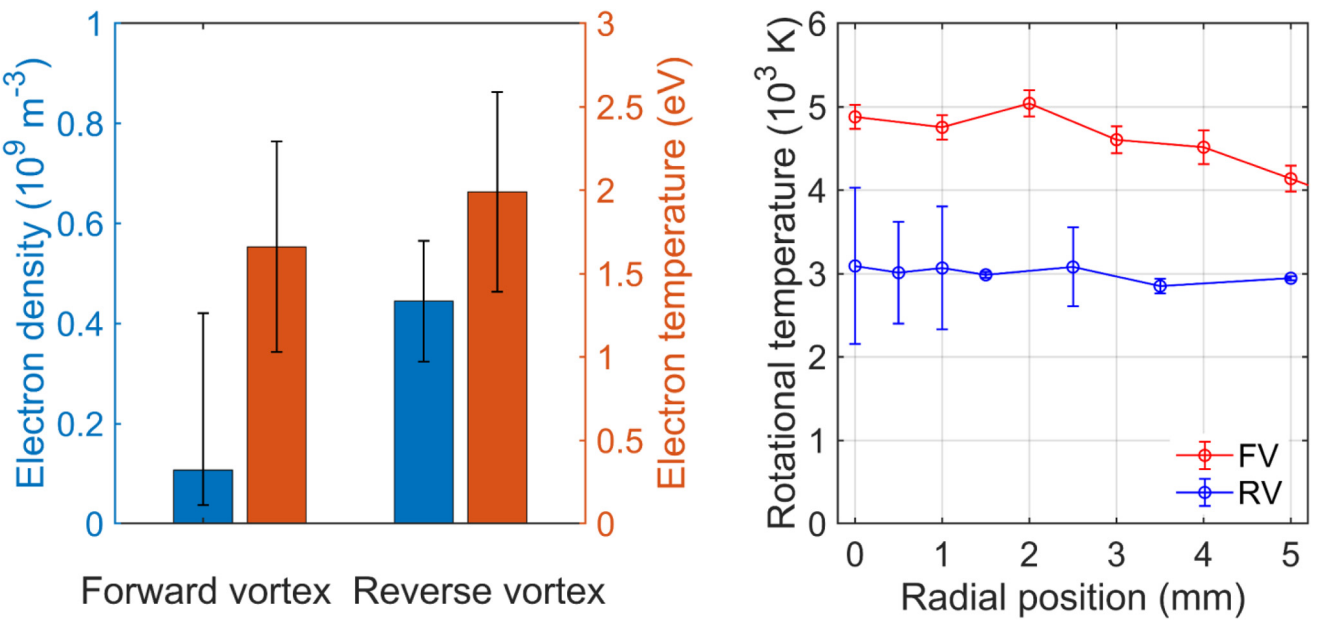

Fig. 4 Electron density and temperature (left) measured at the core of the plasma (averaged over 1 mm) and radial profiles of rotational temperature (right), for 20% CH_4 in the feed gas, in forward and reverse vortex flow configurations (1000 W, 100 mbar, total flow rate of 17 slm).

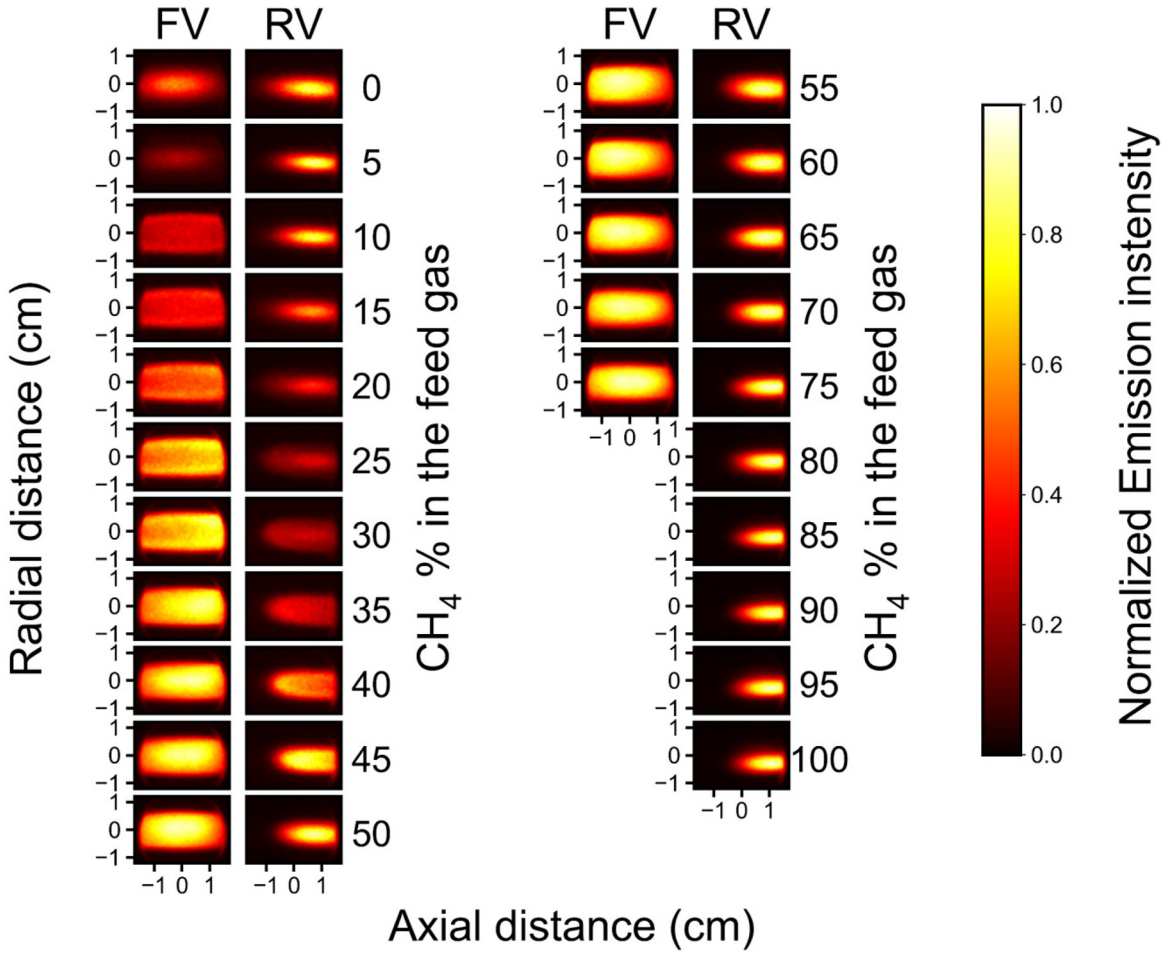

Fig. 5 Normalized optical emission images of the plasma in forward vortex (FV) and reverse vortex (RV) configurations as a function of the CH_4 fraction in the feed gas, with emission intensity normalized at the maximum value in each image (1000 W, 17 slm, 100 mbar).

The principal reaction pathway of the carbon deposition generally follows the Kassel mechanism:[38,39]

$$2CH_4(g) \rightarrow C_2H_6(g) + H_2(g), \text{ with } \Delta H_R^\circ = 67.5\ \text{kJ mol}^{-1} \quad (1)$$

$$C_2H_6(g) \rightarrow C_2H_4(g) + H_2(g), \text{with } \Delta H_R^\circ = 135\ \text{kJ mol}^{-1} \quad (2)$$

$$C_2H_4(g) \rightarrow C_2H_2(g) + H_2(g), \text{with } \Delta H_R^\circ = 173.7\ \text{kJ mol}^{-1} \quad (3)$$

$$C_2H_2(g) \rightarrow 2C(s) + H_2(g), \text{with } \Delta H_R^\circ = -228.8\ \text{kJ mol}^{-1} \quad (4)$$

Primary C_2H_6 is produced through CH_4 dehydrogenation to CH_3 radicals and subsequent CH_3 recombination (eqn (1)); then, a cascade of dehydrogenation reactions to ethylene (eqn (2)), acetylene (eqn (3)) and eventually to solid carbon (eqn (4)) takes place. The last step of the Kassel mechanism (*i.e.* the full dehydrogenation to solid carbon, eqn (4)) is an inherently kinetically limited process, composed of a nucleation step followed by mass growth.[27] Hence, it is promoted by high gas temperatures.

At temperatures exceeding the optimal range for the Kassel mechanism (T_g > 2000 K),[39,40] such as in microwave plasmas, other radical processes may contribute to the formation of C_2H_2 (*e.g.*, hydrogenation of C_2 radicals and CH dimerization)[39,41] and solid carbon (*e.g.*, from C-atom and C_2 condensation),[42] potentially leading to a deviation from the classical Kassel mechanism. However, due to the highly inhomogeneous temperature distribution characteristic of microwave plasmas, an adequate description of the temperature dependence of solid carbon formation can only be made through detailed modelling. Currently, this is very challenging for microwave discharges as it would involve solving chemical kinetics and complex physics (*i.e.* fluid dynamics, heat transfers and microwave absorption) in multidimensions, which is computationally very expensive.

The recirculation cell created in forward vortex configuration (represented by the closed flow lines in Fig. 1) traps the hot gas inside, which can only leave by slow radial diffusion promoted by the onset of strong temperature gradients. This causes an increase in residence time, creating the conditions to form a considerable number of nucleation sites and therefore carbon particles through H-abstraction and C_2H_2 addition (HACA mechanism)[27,43] and/or coagulation.[44] The HACA

 This journal is © The Royal Society of Chemistry 2023

mechanism,[45] depicted in Fig. 6, represents the main growth pathway of aromatic rings in hydrocarbon flames[46,47] and can explain the formation of soot in hydrocarbon-containing plasmas.[48–50] In the latter case, the HACA mechanism is yet to be established, due to the complexity of the plasma environment and the chemistry at play, making the development of detailed kinetic models very challenging. However, Tetard *et al.*[50] performed reactive molecular dynamic simulations to identify the precursors of carbon clusters in an Ar/CH_4, suggesting that C_2H radicals (from C_2H_2 thermal decomposition) are responsible for the formation of large carbon molecules, in line with the HACA mechanism.

The transition from C_2 species to aromatic compounds starts with a linearization process that leads to the formation of the C_4H_3 and C_3H_3 radicals. Then, these radicals undergo cyclization, resulting in the production of the phenyl radical. At this point, the growth of aromatic rings proceeds as shown in Fig. 6.[43,48] This mechanism may be initiated with any large polycyclic aromatic hydrocarbon molecules and results in a molecular growth through the addition of one aromatic ring increase at each step.[48]

Since the size of the resulting carbon particles is significantly larger than the size of the gas molecules, thermophoresis affects their motion to a lesser extent,[51] further increasing their residence time compared to that of the gas in the recirculation cell. Here, carbon particles tend to accumulate and aggregate in larger structures, until they achieve sufficient momentum to leave the closed flow lines and attach to the reactor walls as a result of inertial impaction.[52] A similar behavior was observed for soot particles in C_2H_4 fueled flames, where recirculation zones were created with the aim of trapping the carbon particles and tracking their trajectories inside a vortex flow.[53] Their broadband emission, visible to the naked eye as an orange halo,[33,54] corresponds to the shape of the recirculation cell in our case. The part that is protruding outside the waveguide is not included in the images in Fig. 5. Once the particles are sufficiently heavy and can leave the recirculation cell, they are only *ca.* 6 mm separated from the reactor walls. Under these conditions, solid carbon deposition is thus facilitated, which is indeed very much observed in our experiments in the forward vortex configuration.

In order to find further support to the validity of this mechanism for solid carbon deposition in the forward vortex configuration, in a future study, we will adapt our setup to accommodate instruments for real-time measurement of the concentration of species involved in precursor accumulation, such as C_2H_2, whose concentration can be measured in real time by non-dispersive infrared spectroscopy.[55,56] This will imply the use of specific filters to prevent solid carbon from affecting the functionality of the setup and the quality of the measurements. Additionally, these measurements can be complemented by monitoring the intensity of broadband emission from hot carbon nanoparticles over time. If the time required to reach a steady state between precursor formation and solid carbon deposition is sufficiently long to be captured in continuous measurements, new insights into the mechanisms involved and the effect of solid carbon formation on reactor output can be gained.

In reverse vortex configuration, the transition from O 777 nm to carbon-dominated emission, with a clear change in shape, only appears at *ca.* 30% CH_4 in the feed gas. Nevertheless, the emission zone is limited within a few millimeters in the core of the reactor tube, where the plasma is confined. For reverse vortex configuration, the images in Fig. 3 locate the convective flow in the space, pointing towards the right-hand side, where the gas outlet is located (*cf.* Fig. 1). Unlike in the forward vortex configuration, no broadening of the emission in the radial or axial direction is observed. The lower core T_g and reduced T_g gradients (*cf.* Fig. 4), as a consequence of strong convective cooling, reduce the formation of carbon particles outside the plasma zone.

However, broadband emission due to the carbon particles is still visible, although with much lower intensity compared to the forward vortex configuration for the same CH_4 fraction in the feed gas. This is clear from Fig. 7, which shows the same optical emission images as in Fig. 5, but without normal-

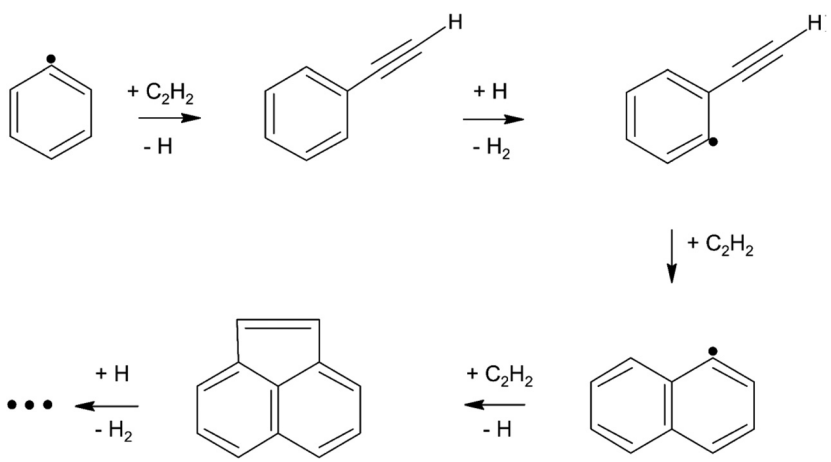

Fig. 6 Schematic of the H-abstraction and C_2H_2 addition mechanism, adapted from Frenklach and Wang.[45]

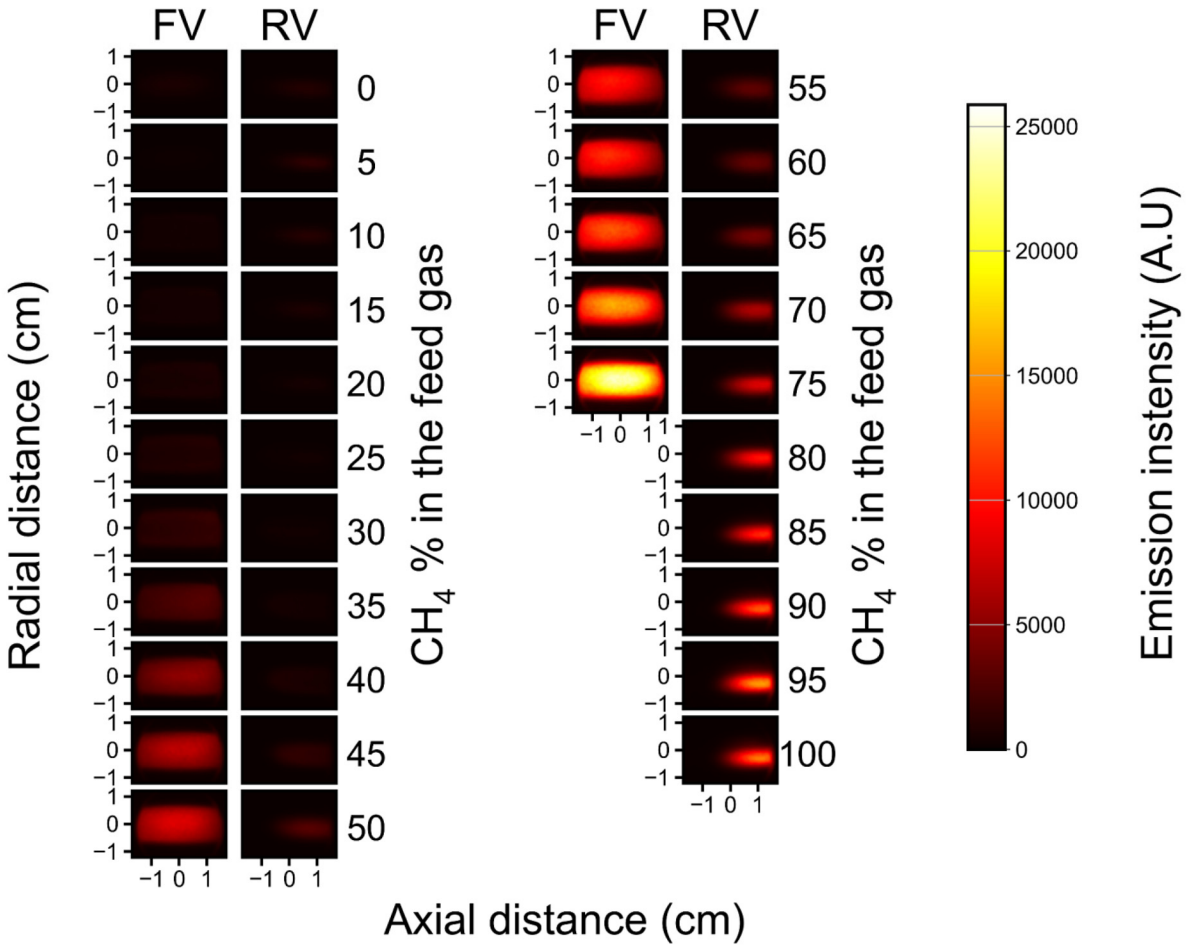

Fig. 7 Optical emission images of the plasma in forward and reverse vortex flow configurations as a function of the CH_4 fraction in the feed gas. The images are recorded with an image intensified CCD high speed camera, with a bandpass filter with a central wavelength of *ca.* 780 nm. In contrast to the images in Fig. 5, here normalization at the maximum value is not applied.

ization at the maximum value in each image. In effect, as illustrated in Fig. 7, the emission intensity increases with the fraction of CH_4. The maximum intensity is achieved at 75% CH_4 in the feed gas in forward vortex flow configuration, right before severe carbon deposition is observed inside the reactor walls, and the plasma shuts off. This clearly links the observed emission with carbon particles.

Interestingly, broadband emission is observed also in reverse vortex flow configuration, where carbon deposition does not occur. However, its intensity is much lower than in the forward vortex configuration for the same conditions, suggesting that the amount (and likely also the size) of carbon particles is substantially reduced. Indeed, the absence of a recirculation zone in the reverse vortex configuration limits the formation of larger and stable carbon aggregates, explaining the lower emission intensity from blackbody radiation, together with no carbon deposition at the walls. Moreover, the hot gas removed from the plasma zone is quickly quenched by the input gas in reverse vortex configuration (*cf.* flow lines in Fig. 1 and Bongers *et al.*[26]). If the cooling is sufficiently fast, mixing with the input gas may further reduce particle aggregation in stable structures downstream the plasma zone, as reported in literature.[27]

Reactor performance

In the previous section, we explored the dynamics of solid carbon deposition and its correlation with flow topology. Building upon these insights, we now shift our focus to the evaluation of the DRM performance in our microwave plasma in both forward and reverse vortex configurations. This analysis aims to infer the effect of the flow geometry on the chemistry. The exhaust composition is reported in Fig. 8 for a range of CO_2/CH_4 mixtures (from pure CO_2 up to pure CH_4).

Fig. 8 (top panel) reveals that, under the experimental conditions studied, the flow rate exerts a more pronounced influence than the flow configuration on both CO_2 and CH_4 conversion. The partial overlapping of the conversion performance of forward and reverse vortex can be ascribed to the higher temperature (see Fig. 4) and residence time (see next section) in the former configuration, which should favor higher conversion, being counteracted by greater gas mixing between the input cold gas and output hot gas, improved heat insulation, and a

 This journal is © The Royal Society of Chemistry 2023

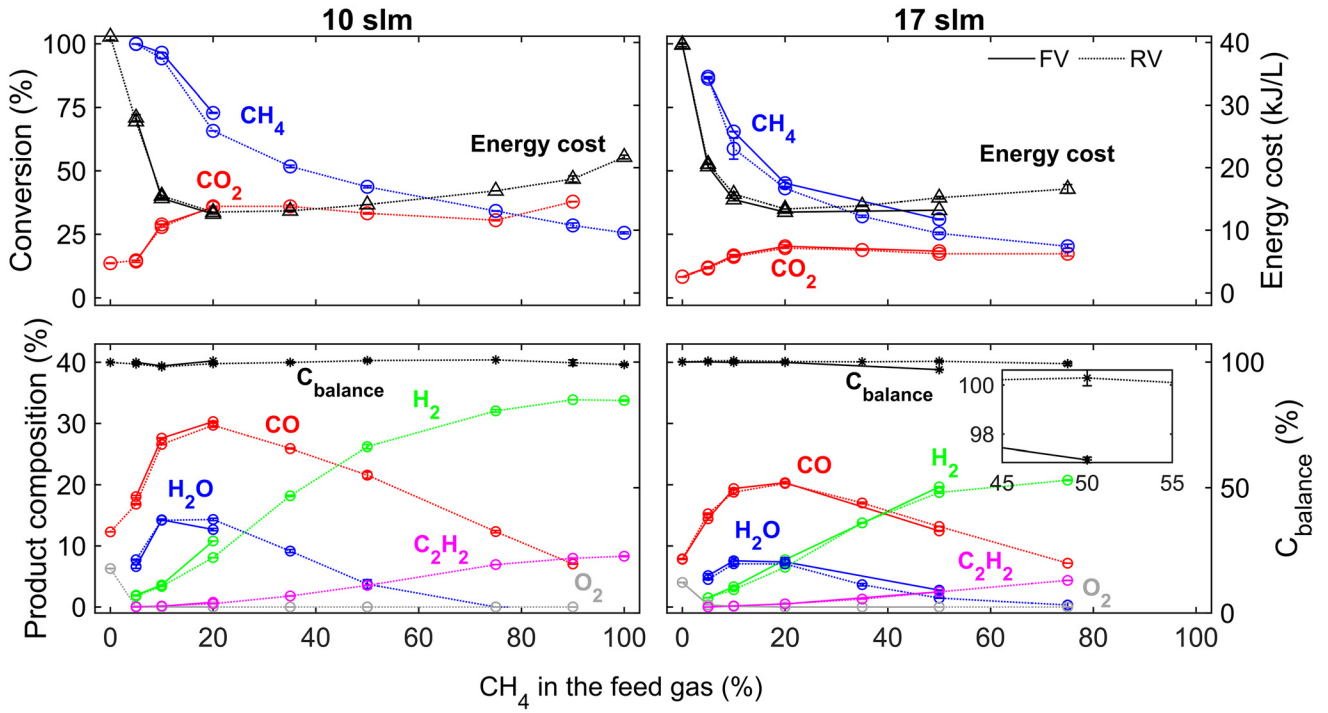

Fig. 8 (Top) CO_2 and CH_4 conversion and energy cost; (bottom) product composition and carbon balance ($C_{balance}$) as a function of the CH_4 fraction in the feed gas, in forward vortex (FV) and reverse vortex (RV) flow configuration, for 10 slm (left) and 17 slm (right) (1000 W, 100 mbar).

higher fraction of gas being treated by the plasma in the latter configuration.[57,58] While the conversion performance is comparable, what is more crucial to note is that operating in the forward vortex configuration becomes unfeasible due to solid carbon formation when CH_4 fractions exceed 20% at 10 slm and 50% at 17 slm. Consequently, there are no data points for these conditions, and plasma instabilities occur at higher CH_4 fractions. This phenomenon can be attributed to the strong microwave absorption capacity of carbon particles,[6] causing a shielding of the microwave power to the plasma. For higher fractions of CH_4 (*i.e.* above 20% and 50% at 10 and 17 slm, respectively), this eventually makes it impossible to maintain a stable discharge.

In stark contrast, the reverse vortex configuration enables stable and solid carbon-free operation up to pure CH_4 feed gas (the lack of data points for CH_4 fractions >75%, at 17 slm was due to inherent limitations of the mass flow controllers in use). This highlights that the flow stagnation in forward vortex leads to reduced mass and heat transfer, higher residence times and thus increased tendency to carbon deposition. *Vice versa*, the reverse vortex configuration allows increasing core transport, with great potential for DRM and perhaps even beyond that, for the chemical industry in the context of CH_4 non-oxidative coupling.

The minimum energy cost, calculated from the total conversion (*i.e.* the weighted average of CO_2 and CH_4 conversions), is achieved for 20% CH_4 fraction in the feed gas for all sets of measurements, with the lowest value being 12.6 kJ L^{-1}. At 50% CH_4, the lowest energy cost is 13.2 kJ L^{-1} in forward vortex configuration. In reverse vortex configuration, this increases to 14.1 kJ L^{-1} at 10 slm and to 15.1 kJ L^{-1} at 17 slm. For comparison, Chun *et al.*[16] and Sun *et al.*[17] achieved an energy cost of 14.5 kJ L^{-1} and 12.8 kJ L^{-1}, respectively, for CO_2/CH_4 50/50 microwave plasma. It is important to acknowledge that, depending on the application, achieving full conversion may be more crucial than minimizing the energy cost of syngas production. In practice, insufficient conversion performance results in low-quality reactor output, increasing the separation costs and constraining resource utilization. In this regard, Chun *et al.*[16] and Sun *et al.*[17] demonstrated that plasma-based DRM can attain nearly complete CH_4 conversion (and also CO_2 conversion for Sun *et al.*[17]), albeit with the production of solid carbon. Future developments will focus on characterizing the performance of the microwave reactor in reverse vortex across a wider parameter space, aiming at finding conditions where full reactant conversion coincides with the elimination of solid carbon formation. This investigation will omit the use of a laser scattering device, employed in this study to link macroscopic observations to plasma properties and T_g. The presence of the laser beam at the center of the reactor tube precludes the use of nozzles to further stabilize the reverse vortex configuration. These nozzles force gas mixing and fast quenching of the output gas, further enhancing the conversion performance. Moreover, the presence of the laser makes it difficult to conduct experiments at pressures close to atmospheric, which would be more relevant for industrial applications and may results even in higher conversion, as shown by Hecimovic *et al.*[58] for pure CO_2.

The product composition (Fig. 8, bottom panel) mainly consists of syngas (H_2 and CO), along with H_2O (whose concentration is estimated from the O balance, as described by Wanten *et al.*[2]) and C_2H_2. The addition of 5% CH_4 in the feed gas removes O_2 from the output stream.

Just like the conversion rates, the product distribution remains nearly unchanged regardless of the flow configuration. The same pattern is observed in the volumetric production rates, as shown in the ESI (section 2; Fig. S1†). This behavior can be attributed to the fact that the gas residence time in the hot zone falls within the optimal range for C_2H_2 production from methane pyrolysis in both configurations (see next section), *i.e.* 10^{-4}–10^{-3} s,[27] while for temperatures exceeding 1000 K, syngas is the main product of DRM.[59,60] The higher temperature in forward vortex than in reverse vortex leads to higher production of radicals and atomic species in the hot plasma core, which then recombine into C_2H_2, syngas and solid carbon precursors. This decomposition into smaller species is decreased by the lower temperature in reverse vortex, but this does not alter the final composition of the products under the experimental conditions tested in this study. Additionally, the carbon balance ($C_{balance}$) consistently approaches 100% within the error margins. A small deviation (*ca.* 97%) is only observed for the case of 50% CH_4 in the feed gas with forward vortex flow at 17 slm. Recently, Kelly *et al.*[55] conducted DRM experiments in a microwave plasma with a swirling flow configuration, 1 kW power, 10 slm total gas flow, and atmospheric pressure. They collected and characterized solid carbon samples, revealing a "carbon black" type material composed of pure, largely amorphous carbon with a mean particle size of 20 nm. Given the very similar experimental conditions, we expect that the solid carbon produced during our experiments will have analogous characteristics. Thus, the discrepancy in carbon balance, or carbon loss, that we observed can be directly correlated to a deposition rate of around 25 mg min^{-1} of solid material. While this rate is sufficient to be visible, it does not lead to operational instabilities within the timeframe of each experiment (*e.g.* 10 minutes). However, as we advocate for the scaling up of plasma-based DRM, additional tests will be necessary to evaluate the stability of the process for longer timeframes (*i.e.* >1 h). To this end, the use of specific filters to collect and weigh solid carbon after the plasma will be beneficial. This allows for the quantification of the carbon losses even under conditions where the deviation of the carbon balance from 100% is minimal. Indeed, such small deviations, if persistent over many hours of operation, could potentially lead to operational issues. Analogously, it is essential to note that even small amounts of carbon deposition can cause significant damage to the GC. As a result, we refrained from measuring the exhaust composition for higher CH_4 fractions in the forward vortex configuration. In practice, for CH_4 fractions exceeding 50%, we observe substantial deposition along with plasma instability, and we anticipate more substantial deviations in carbon balance. Hence, despite the absence of apparent differences in gaseous product distributions in Fig. 8, specifically for CH_4 fractions below 50%, it is clear that the reverse and forward vortex configurations significantly differ in terms of solid carbon deposition. This distinction becomes especially pronounced at higher CH_4 fractions in the feed gas.

Inhibition of solid carbon deposition

In the preceding sections, we uncovered the crucial role of flow topology in inhibiting carbon deposition and reshaping the kinetics of methane decomposition. In this section, we examine the DRM chemistry at high T_g and its direct correlation with the occurrence of carbon deposition. As outlined earlier, solid carbon deposition in DRM arises from the same mechanism as in pure CH_4 splitting, *i.e.* from (oxidative) hydrocarbon pyrolysis.[13] According to the Kassel mechanism[38,39] (see eqn (1)–(4) in section 3.2 above), CH_3 radicals formed upon dissociation of CH_4 recombine to form C_2H_6 (eqn (1)). After that, a cascade of dehydrogenation reactions to C_2H_4 (within 10^{-6}–10^{-5} s, eqn (2)), C_2H_2 (10^{-4}–10^{-3} s, eqn (3)) and eventually to solid carbon (eqn (4)) takes place, depending on the residence time in the reaction zone.

The only C_2 hydrocarbon detected in our measurements is C_2H_2, indicating that the residence time is likely in the millisecond range in both forward and reverse vortex configurations. Calculations by van de Steeg[23] indicate convection velocities of approximately 150 m s^{-1} in the reverse vortex configuration, in contrast to diffusion velocities of about 5 m s^{-1} in the forward vortex configuration, for pure CO_2 under similar conditions.

In the reverse vortex setup, the convective flow is oriented towards the gas outlet. If we take a plasma length of *ca.* 2 cm, as estimated from the plasma images (*cf.* section 3 in the ESI†), the resulting residence time is *ca.* 0.1 ms. Conversely, the forward vortex configuration is characterized by diffusive flow going mainly from the core towards the outer vortex. Hence, with a plasma radius of *ca.* 0.4 cm (see again section 3 of the ESI†), the estimated residence time is *ca.* 0.8 ms. However, if we consider the interface between the inner recirculation cell and the outer vortex, which is at *ca.* 0.7 cm from the core (*cf.* Fig. 5), then the residence time is *ca.* 1.4 ms, *i.e.* one order of magnitude longer than in reverse vortex configuration.

In effect, in the forward vortex configuration, the gas is trapped inside a recirculation cell with closed flow lines (*cf.* Fig. 1), in which the plasma is stabilized, and can only leave through radial transport, as demonstrated before.[22,24] This process is much slower than convection, which dominates core transport in reverse vortex configuration, in line with previous work.[23,24] Hence, the difference in estimated residence time, arising from the characteristic flow configuration, can explain the absence of carbon deposition in the reverse vortex configuration.

For the conditions tested during the GC campaign, *i.e.* CH_4 fractions ≤50% in forward vortex configuration, only primary carbon particles are formed, with limited aggregation and thus with negligible contribution to the carbon balance. For high fractions of CH_4, the particles can form larger aggregates, car-

 This journal is © The Royal Society of Chemistry 2023

rying a larger momentum and eventually depositing at the inner walls of the quartz tube. In these conditions, losses to solid deposits may have a much larger contribution to the carbon balance. In effect, above 75% CH_4 in the feed gas, the plasma is not stable anymore and it quickly shuts off. This is ascribed to a prominent formation of carbon particles, as demonstrated by Fig. 7, which absorb the microwaves and shields the microwave power from the plasma.

Therefore, we hypothesize that the substantial inhibition of carbon deposition in the reverse vortex configuration arises from the specific flow topology, which determines the trajectory of the solid carbon precursors and their ability to aggregate and reach the reactor walls. Optical emission images show that carbon particles are formed in both flow configurations, although they have little contribution to the carbon balance until solid deposits are formed. The shorter residence time in the hot zone in reverse vortex configuration, together with the absence of a recirculation cell, determines the possibility to operate in a solid-carbon free regime even under conditions where solid carbon formation would be thermodynamically favorable.[27] Consequently, the flow topology affects the chemistry, and for CH_4 decomposition it determines a shift from a kinetics dominated by full (oxidative) pyrolysis ($CH_4 \rightarrow C_s + 2\ H_2$) towards a larger contribution from partial pyrolysis ($2\ CH_4 \rightarrow C_2H_2 + 3\ H_2$), without any other parametric modification. The shift is not captured by the GC analysis because conditions of severe carbon deposition are avoided to preserve the functionality of the diagnostics. However, the shift is observable from our experiments performed without the limitations imposed by the diagnostics, in which the plasma stability in forward vortex configuration is hampered by the large amount of solid carbon deposition. Hence, the insight provided by this work represents an important step further in the understanding and, therefore, control of the process, from which future efforts in scaling up of plasma-based DRM (and CH_4 non-oxidative coupling) can benefit.

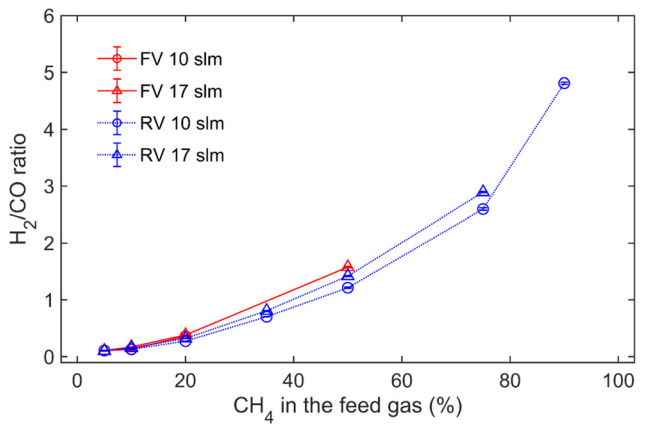

Fig. 9 Syngas (H_2/CO) ratio as a function of the CH_4 fraction in the feed gas in the forward vortex (FV) and reverse vortex (RV) configuration, at 10 and 17 slm (100 mbar, 1000 W).

In essence, we demonstrate that the reverse vortex configuration avoids carbon deposition and hence provides the opportunity of fully exploiting the DRM chemistry, from low fractions of CH_4 in the feed gas up to pure CH_4, and therefore achieving solid carbon-free syngas at the desired ratios, as shown in Fig. 9. For instance, a H_2/CO ratio of 2 is desired for methanol and Fisher-Tropsch synthesis, which is potentially attainable with a CH_4 fraction of *ca.* 60% in reverse vortex configuration, without the use of a catalyst.

Conclusions

Our work illustrates the essential role of the flow dynamics (reverse *vs.* forward vortex) in avoiding solid carbon deposition in complex mixtures such as CO_2/CH_4. The strong convective core-periphery transport characterizing the reverse vortex flow configuration significantly reduces the formation and growth of solid carbon precursors, and inhibits their deposition at the reactor walls. Therefore, this configuration enables full exploitation of the DRM chemistry, up to very high CH_4/CO_2 ratios, which were thus far impossible, due to severe solid carbon deposition. Furthermore, the reverse vortex configuration seems very promising for non-oxidative coupling of CH_4 to higher-value hydrocarbons (*e.g.*, C_2H_2 and C_2H_4), as the core temperature can be reduced, thus shifting the chemistry towards partial pyrolysis of CH_4. Indeed, we hope to achieve steering of the selectivity towards higher-value hydrocarbons by properly optimizing the reactor configuration and exploring a wider parameter space, especially higher flow rates and pressures in combination with varying power input. This level of control is challenging to achieve in the forward vortex configuration, primarily due to restricted influence over residence time in the hot plasma zone. Moreover, the reverse vortex configuration opens up the intriguing possibility of sustaining a microwave plasma in non-thermal equilibrium (*i.e.* with $T_e > T_g$). This is achieved through intense core-periphery convection, effectively cooling down the discharge zone. This can be beneficial for the production of C_2 hydrocarbons or heavier molecules, whose formation is limited by the high T_g in thermal plasmas. These hypotheses will be subject of future investigation within our groups.

Author contributions

Conceptualization, O.B., G.v.R. and A.B.; methodology & investigation, O.B., C.v.D., A.H. and A.v.d.S.; writing – original draft, O.B. and C.v.D.; writing – review & editing, O.B., C.v.D., A.H., A.v.d.S., W.B., M.C.M.v.d.S., G.v.R. and A.B.; funding acquisition & resources, M.C.M.v.d.S., G.v.R. and A.B.; supervision, G.v.R. and A.B.

Conflicts of interest

There are no conflicts to declare.

Acknowledgements

The authors would like to thank Bart Wanten for the kind help in the analysis of the data. This research was supported by the European Union's Horizon 2020 Research and Innovation Programme under the Marie Sklodowska-Curie Grant Agreement No. 813393 (PIONEER) and the SEP-BOF project of UAntwerpen. This work used the plasma setup of the Power to Gas (P2G) open technology research programme with project number 15325, which is co-financed by the Netherlands Organisation for Scientific Research (NWO), Gasunie, Ampleon, Stedin and DNVGL.

References

1 R. Snoeckx and A. Bogaerts, *Chem. Soc. Rev.*, 2017, **46**, 5805–5863.
2 B. Wanten, S. Maerivoet, C. Vantomme, J. Slaets, G. Trenchev and A. Bogaerts, *J. CO2 Util.*, 2022, **56**, 101869.
3 G. Henrici-Olivé and S. Olivé, *Angew. Chem., Int. Ed. Engl.*, 1976, **15**, 136–141.
4 M. J. Bos, S. R. A. Kersten and D. W. F. Brilman, *Appl. Energy*, 2020, **264**, 114672.
5 J. Ma, M. Fang, P. Li, B. Zhu, X. Lu and N. T. Lau, *Appl. Catal., A*, 1997, **159**, 211–228.
6 J. A. Menéndez, A. Arenillas, B. Fidalgo, Y. Fernández, L. Zubizarreta, E. G. Calvo and J. M. Bermúdez, *Fuel Process. Technol.*, 2010, **91**, 1–8.
7 Z. Bo, J. Yan, X. Li, Y. Chi and K. Cen, *Int. J. Hydrogen Energy*, 2008, **33**, 5545–5553.
8 S. B. Shenoy, A. Rabinovich, A. Fridman and H. Pearlman, *Plasma Processes Polym.*, 2019, **16**, 1800159.
9 O. Muraza and A. Galadima, *Int. J. Energy Res.*, 2015, **39**, 1196–1216.
10 H. Puliyalil, D. Lašič Jurković, V. D. B. C. Dasireddy and B. Likozar, *RSC Adv.*, 2018, **8**, 27481–27508.
11 D. Lašič Jurković, J.-L. Liu, A. Pohar and B. Likozar, *Catal. Today*, 2021, **362**, 11–21.
12 D. Lašič Jurković, H. Puliyalil, A. Pohar and B. Likozar, *Int. J. Energy Res.*, 2019, **43**, 8085–8099.
13 L. C. S. Kahle, T. Roussière, L. Maier, K. Herrera Delgado, G. Wasserschaff, S. A. Schunk and O. Deutschmann, *Ind. Eng. Chem. Res.*, 2013, **52**, 11920–11930.
14 Q. Chen, J. H. B. J. Hoebink and G. B. Marin, *Ind. Eng. Chem. Res.*, 1991, **30**, 2088–2097.
15 M. Scapinello, L. M. Martini, G. Dilecce and P. Tosi, *J. Phys. D: Appl. Phys.*, 2016, **49**, 075602.
16 S. M. Chun, Y. C. Hong and D. H. Choi, *J. CO2 Util.*, 2017, **19**, 221–229.
17 H. Sun, J. Lee and M. S. Bak, *J. CO2 Util.*, 2021, **46**, 101464.
18 D. K. Dinh, G. Trenchev, D. H. Lee and A. Bogaerts, *J. CO2 Util.*, 2020, **42**, 101352.
19 J. Liu, Z. Xue, Z. Zhang, B. Sun and A. Zhu, *Plasma Processes Polym.*, 2023, **20**(4), 2200175.
20 J.-L. Liu, H.-W. Park, W.-J. Chung and D.-W. Park, *Plasma Chem. Plasma Process.*, 2016, **36**, 437–449.
21 S. Van Alphen, J. Slaets, S. Ceulemans, M. Aghaei, R. Snyders and A. Bogaerts, *J. CO2 Util.*, 2021, **54**, 101767.
22 A. J. Wolf, F. J. J. Peeters, P. W. C. Groen, W. A. Bongers and M. C. M. van de Sanden, *J. Phys. Chem. C*, 2020, **124**, 16806–16819.
23 A. W. van de Steeg, *Insight into CO_2 Dissociation Kinetics in Microwave Plasma using Laser Scattering*, Eindhoven University of Technology, 2022.
24 A. Gutsol and J. A. Bakken, *J. Phys. D: Appl. Phys.*, 1998, **31**, 704–711.
25 G. Trenchev, S. Kolev and A. Bogaerts, *Plasma Sources Sci. Technol.*, 2016, **25**, 035014.
26 W. Bongers, H. Bouwmeester, B. Wolf, F. Peeters, S. Welzel, D. van den Bekerom, N. den Harder, A. Goede, M. Graswinckel, P. W. Groen, J. Kopecki, M. Leins, G. van Rooij, A. Schulz, M. Walker and R. van de Sanden, *Plasma Processes Polym.*, 2017, **14**, 1600126.
27 J. R. Fincke, R. P. Anderson, T. A. Hyde and B. A. Detering, *Ind. Eng. Chem. Res.*, 2002, **41**, 1425–1435.
28 N. den Harder, D. C. M. van den Bekerom, R. S. Al, M. F. Graswinckel, J. M. Palomares, F. J. J. Peeters, S. Ponduri, T. Minea, W. A. Bongers, M. C. M. van de Sanden and G. J. van Rooij, *Plasma Processes Polym.*, 2017, **14**, 1600120.
29 A. W. van de Steeg, L. Vialetto, A. F. S. da Silva, P. Viegas, P. Diomede, M. C. M. van de Sanden and G. J. van Rooij, *J. Phys. Chem. Lett.*, 2022, **13**, 1203–1208.
30 A. J. Wolf, T. W. H. Righart, F. J. J. Peeters, P. W. C. Groen, M. C. M. van de Sanden and W. A. Bongers, *Plasma Sources Sci. Technol.*, 2019, **28**, 115022.
31 P. Viegas, L. Vialetto, A. W. van de Steeg, A. J. Wolf, W. A. Bongers, G. J. van Rooij, M. C. M. van de Sanden, P. Diomede and F. J. J. Peeters, *Plasma Sources Sci. Technol.*, 2021, **30**, 065022.
32 M. A. Elliott, P. W. May, J. Petherbridge, S. M. Leeds, M. N. R. Ashfold and W. N. Wang, *Diamond Relat. Mater.*, 2000, **9**, 311–316.
33 A. P. Bolshakov, V. G. Ralchenko, V. Y. Yurov, A. F. Popovich, I. A. Antonova, A. A. Khomich, E. E. Ashkinazi, S. G. Ryzhkov, A. V. Vlasov and A. V. Khomich, *Diamond Relat. Mater.*, 2016, **62**, 49–57.
34 A. Mohanta, B. Lanfant, M. Asfaha and M. Leparoux, *J. Phys.: Conf. Ser.*, 2017, **825**, 012010.
35 J. Oliver, N. Bharadwaj and T. Sizyuk, *J. Appl. Phys.*, 2019, **125**, 073301.
36 S. H. Zaidi, Z. Tang, A. P. Yalin, P. Barker and R. B. Miles, *AIAA J.*, 2002, **40**, 1087–1093.
37 B. L. M. Klarenaar, F. Brehmer, S. Welzel, H. J. van der Meiden, M. C. M. van de Sanden and R. Engeln, *Rev. Sci. Instrum.*, 2015, **86**, 046106.
38 L. S. Kassel, *J. Am. Chem. Soc.*, 1932, **54**, 3949–3961.
39 M. Scapinello, E. Delikonstantis and G. D. Stefanidis, *Chem. Eng. Process.*, 2017, **117**, 120–140.
40 M. Dors, H. Nowakowska, M. Jasiński and J. Mizeraczyk, *Plasma Chem. Plasma Process.*, 2014, **34**, 313–326.

 This journal is © The Royal Society of Chemistry 2023

41 D. H. Lee, K.-T. Kim, Y.-H. Song, W. S. Kang and S. Jo, *Plasma Chem. Plasma Process.*, 2013, **33**, 249–269.
42 R. Vander Wal, A. Sengupta, E. Musselman and G. Skoptsov, *C*, 2018, **4**, 61.
43 H. Wang and M. Frenklach, *Combust. Flame*, 1997, **110**, 173–221.
44 J. W. Martin, M. Salamanca and M. Kraft, *Prog. Energy Combust. Sci.*, 2022, **88**, 100956.
45 M. Frenklach and H. Wang, *Aromatics growth beyond the first ring and the nucleation of soot particles*, Department of Materials Science and Engineering, The Pennsylvania State University, 1991.
46 J. A. Miller, R. J. Kee and C. K. Westbrook, *Annu. Rev. Phys. Chem.*, 1990, **41**, 345–387.
47 M. Frenklach and A. M. Mebel, *Phys. Chem. Chem. Phys.*, 2020, **22**, 5314–5331.
48 K. Hassouni, F. Mohasseb, F. Bénédic, G. Lombardi and A. Gicquel, *Pure Appl. Chem.*, 2006, **78**, 1127–1145.
49 B. Yan, Y. Cheng, T. Li and Y. Cheng, *Energy*, 2017, **121**, 10–20.
50 G. Tetard, A. Michau, S. Prasanna, J. Mougenot, P. Brault and K. Hassouni, *Plasma Processes Polym.*, 2022, **19**, 2100204.
51 R. R. Devetyarov, *IOP Conf. Ser.: Mater. Sci. Eng.*, 2020, **862**, 062072.
52 M. H. Pourrezaei, M. R. Malayeri and K. Hooman, *Int. J. Therm. Sci.*, 2019, **146**, 106108.
53 W. M. Roquemore, V. Katta, S. Stouffer, V. Belovich, R. Pawlik, M. Arstingstall, G. Justinger, J. Gord, A. Lynch, J. Zelina and S. Roy, *Proc. Combust. Inst*, 2009, 32, 729–736.
54 N. Derkaoui, C. Rond, K. Hassouni and A. Gicquel, *J. Appl. Phys.*, 2014, **115**, 233301.
55 S. Kelly, E. Mercer, R. De Meyer, R.-G. Ciocarlan, S. Bals and A. Bogaerts, *J. CO2 Util.*, 2023, **75**, 102564.
56 L. Fulcheri, V.-J. Rohani, E. Wyse, N. Hardman and E. Dames, *Int. J. Hydrogen Energy*, 2023, **48**, 2920–2928.
57 T. Nunnally, K. Gutsol, A. Rabinovich, A. Fridman, A. Gutsol and A. Kemoun, *J. Phys. D: Appl. Phys.*, 2011, **44**, 274009.
58 A. Hecimovic, C. K. Kiefer, A. Meindl, R. Antunes and U. Fantz, *J. CO2 Util.*, 2023, **71**, 102473.
59 M. Usman, W. M. A. W. Daud and H. F. Abbas, *Renewable Sustainable Energy Rev.*, 2015, **45**, 710–744.
60 J. Martin-del-Campo, S. Coulombe and J. Kopyscinski, *Plasma Chem. Plasma Process.*, 2020, **40**, 857–881.